Nano Today 34 (2020) 100908

Contents lists available at ScienceDirect

Nano Today

journal homepage: www.elsevier.com/locate/nanotoday

Wafer-scale growth of single-crystal graphene on vicinal Ge(001) substrate

Panlin Li[a,d,1], Wenya Wei[b,c,1], Miao Zhang[a], Yongfeng Mei[e], Paul K. Chu[f], Xiaoming Xie[a], Qinghong Yuan[b,c,**], Zengfeng Di[a,*]

[a] State Key Laboratory of Functional Materials for Informatics, Shanghai Institute of Microsystem and Information Technology, Chinese Academy of Sciences, Shanghai 200050, China
[b] State Key Laboratory of Precision Spectroscopy, School of Physics and Material Science, East China Normal University, Shanghai 200062, China
[c] Centre for Theoretical and Computational Molecular Science, Australian Institute for Bioengineering and Nanotechnology, The University of Queensland, Brisbane, QLD, 4072, Australia
[d] Center of Materials Science and Optoelectronics Engineering, University of Chinese Academy of Sciences, Beijing 100049, China
[e] Department of Materials Science, Fudan University, Shanghai 200433, China
[f] Department of Physics, Department of Materials Science & Engineering, Department of Biomedical Engineering, City University of Hong Kong, Tat Chee Avenue, Kowloon, Hong Kong, China

ARTICLE INFO

Article history:
Received 3 March 2020
Received in revised form 14 May 2020
Accepted 3 June 2020
Available online 20 June 2020

Keywords:
Graphene
Alignment
Single-crystal
Miscut angle
THz-TDS

ABSTRACT

Wafer-scale single-crystal graphene with high carrier mobility is essential as a promising channel material for the next-generation two-dimensional nanoelectronics. However, direct synthesis of wafer-scale single-crystal graphene on complementary metal oxide semiconductor (CMOS) compatible substrates still remains a challenge. Herein, we demonstrate that single-crystal graphene film with high mobility can be synthesized on the 15° miscut Ge(001) surface by perfectly aligning all the graphene islands and this feat has never been achieved on the normal Ge(001) surface. Both experimental observations and theoretical calculations suggest unidirectional alignment of the graphene islands on the 15° miscut Ge(001) surface is caused by suppression of graphene nucleation along the miscut direction of the vicinal surface. *Ex situ* atomic force microscopy (AFM) verifies that no additional graphene island nucleates after the initial nucleation process and wafer-scale single-crystal graphene is formed by the seamless stitching of the preferentially oriented graphene islands. The obtained wafer-scale single-crystal graphene possesses an ultrahigh carrier mobility, opening an avenue toward scalable fabrication of two-dimensional nanoelectronic devices based on single-crystal graphene without grain boundaries.

Introduction

Graphene, a perfect two-dimensional carbon material, has attracted global interest due to its exceptional chemical stability, superior mechanical stability, and extremely high carrier mobility. In particular, wafer-scale single-crystal graphene with high mobility is crucial for massive production of graphene based nanoelectronic devices and circuits. However, grain boundaries (GBs) are usually formed inevitably in graphene during the chemical vapor deposition (CVD) process [1–8]. Some progress has been made regarding the growth of single-crystal graphene films on metal catalysts such as Cu [9–17] and Cu-Ni alloy [18–22], but the mainstream integrated circuit (IC) technology requires metal-free single-crystal graphene on CMOS compatible substrate. In recent years, semiconducting Ge wafer has been successfully utilized as a proper substrate for the epitaxial growth of graphene due to its catalytic activity and low solubility of carbon [23]. Integration of graphene with Ge substrates by the epitaxial growth approach may address the scarcity issue of IC-compatible graphene wafers and promote the development of graphene-based nanoelectronic devices and circuits.

Wafer-scale single-crystal graphene film was firstly synthesized on 2-inch Ge substrate with the unusual (110) orientation by Lee et al. [24]. Our previous study further discovered that the formation of well-aligned graphene islands, which are seamlessly stitched to form a single-crystal graphene film, was caused by the lat-

* Corresponding author.
** Corresponding author at: State Key Laboratory of Precision Spectroscopy, School of Physics and Material Science, East China Normal University, Shanghai 200062, China.
E-mail addresses: qinghong.yuan@uq.edu.au (Q. Yuan), zfdi@mail.sim.ac.cn (Z. Di).
[1] These authors contributed equally to this work.

https://doi.org/10.1016/j.nantod.2020.100908
1748-0132/

tice matching between the graphene islands and natural atomic steps on the Ge(110) surface [25]. However, the mainstream CMOS technology is mainly based on Si wafers with the usual (001) orientation. Considering the conventional Ge epilayer on Si substrate, the Ge(001) substrate is more compatible with the standard Si-based CMOS process compared to Ge(110). The pioneer study on graphene grown on Ge(001) found that graphene nanoribbons (GNRs) with a high aspect ratio and preferential orientation were always formed along the two perpendicular Ge<110> directions [26,27]. GNRs with an equivalent population in the orthogonal orientations lead to the formation of numerous GBs when GNRs expand to merge into a continuous wafer-scale film, which will degrade the performance of graphene-based nanoelectronic devices and circuits. Recently, much efforts, including H_2/CH_4 flow ratio optimization [28] and vicinal Ge(001) substrate [29,30], have been made to improve the crystal quality of graphene on Ge(001) wafers. However, the formation of GBs could not be fully suppressed by optimizing H_2/CH_4 flow ratio. Meanwhile, the miscut angle of vicinal Ge(001) substrate was found to affect the orientations of GNRs, however the expected well-aligned GNRs together with the consequent seamless stitching to form a single-crystal graphene wafer has not been demonstrated due to the limited variation of miscut angle of vicinal Ge(001) wafer.

Herein, using vicinal Ge(001) substrate with a miscut angle of 10° or above, unidirectional alignment of graphene islands is achieved and the wafer-scale single-crystal graphene realized by the seamless stitching of well aligned graphene islands is demonstrated on the 15° miscut Ge(001) surface. Both experimental data and theoretical calculations show that the nucleation orientation selectivity of graphene islands closely correlates with the miscut angle of the vicinal Ge(001) surface. Complete suppression of GNR nucleation along the miscut direction is observed from the vicinal Ge(001) surface with a miscut angle of 15°, while aligned graphene islands perpendicular to the miscut direction are maintained. Furthermore, the designed *ex situ* AFM indicates no additional graphene islands nucleate after the initial nucleation process, and the wafer-scale single-crystal graphene is formed by the merging of aligned graphene islands after the island expansion. The obtained single-crystal graphene wafer possesses an ultrahigh carrier mobility comparable to that of exfoliated graphene, as evident by terahertz time-domain spectroscopy (THz-TDS), which constitutes a significant advance toward the manufacturing of graphene-based nanoelectronic devices and circuits.

Material and methods

Graphene growth

The vicinal Ge(001) substrates with various miscut angles toward [111] direction were loaded into a horizontal quartz tube. The quartz tube was evacuated to about 10^{-6} bar, and then refilled with argon (Ar, 99.9999 % purity) and hydrogen (H_2, 99.9999 % purity) to reach atmospheric pressure. The chamber was heated to 916 °C with Ar and H_2 for 1 h and then methane (CH_4, 99.99 % purity) was introduced to initiate graphene growth. Afterwards, the flow of CH_4 was shut off and the furnace was cooled down to room temperature under the protection of Ar and H_2 mixture. It should be noted that the growth of graphene on Ge substrate is self-limited and monolayer graphene is always formed due to the ultralow solubility of carbon in Ge [23,24].

Graphene transfer

To transfer the graphene film from the Ge substrate to a target substrate for Raman and High Resolution-Transmission Electron Microscope (HR-TEM) measurement, poly(methyl methacrylate) (PMMA) was spin-coated onto the graphene/Ge substrate and baked at 150 °C for 10 min. After the removal of Ge substrate by the etchant consisting of 1:1:20 H_2O_2:HF:H_2O, a free-standing PMMA/graphene film was obtained, which was further transferred to the target substrate. As PMMA film was removed with acetone, the graphene film was transferred onto the target substrate finally.

DFT calculations

All calculations were performed within the framework of Density Functional Theory (DFT), implemented in the Vienna Ab initio Simulation Package (VASP) [31]. The Generalized Gradient Approximation (GGA) [32] with the Perdew-Burke-Ernzerhof (PBE) exchange-correlation function was used with the plane-wave cutoff energy set at 400 eV for all calculations. The vdW correction proposed by Grimme (DFT-D2) was used to describe the long-range vdW interactions between graphene and the Ge(001) substrate [33–35]. The vacuum space was set to be at least 15 Å to eliminate the interaction between the neighboring layers. The vicinal Ge(001) substrate was modeled by a periodic slab consisting of at least five atomic layers and the bottom two layers were fixed to mimic the bulk. A supercell size of $42.6 \times 8.52 \times 30$ Å^3 was used to mimic the vicinal Ge(001) surface structures, and the Brillouin zone was sampled by Gamma point. In order to make the lattice size to be calculable, the substrate was stretched slightly (6.4 %) to match the lattice of graphene. The surface Ge atoms except those passivated by graphene edge were passivated by H atoms, as evident by the experimental observation [24,36]. The geometries of the structures were relaxed until the force on each atom was less than 0.01 eV/Å, and the energy convergence criteria of 1×10^{-5} eV was reached.

Characterization

The miscut angles of Ge substrates (175 μm, AXT) were determined using X-ray diffraction (XRD, Philips X'pert) by measuring the maximum angle between the (004) plane and the specular direction [29], as listed in Table S1. The surface morphology of graphene was examined by AFM (Bruker Multimode 8) in the lateral force mode using SNL-10 AFM tips. Raman spectra (Jobin Yvon HR800) were collected to determine the thickness, uniformity, and quality of graphene films using Ar^+ laser with a wavelength of 514 nm and a spot size of 1 μm. The microstructure and crystallinity of the graphene film were characterized by HR-TEM (JEOL JEM-ARM300 F) at 80 kV.

Ex situ *experiments*

The graphene sheets mechanically exfoliated from highly oriented pyrolytic graphite (HOPG) crystals with Scotch tape were intentionally utilized as markers to enable *ex situ* observations. Prior to the growth of graphene, the graphene sheet markers were transferred to the target Ge substrates and annealed under 23 sccm H_2 and 220 sccm Ar at 916 °C for 1 h to remove the possible contamination and strengthen the adhesion between the graphene sheet markers and Ge surface. Then, graphene sheet marker mounted Ge substrate was transferred into a horizontal quartz tube for the growth of graphene. For e*x situ* observations to monitor the graphene growth behavior, the whole process was intentionally divided into several intervals, and the sequential AFM tests focusing on the identical region adjacent to graphene sheet marker were accomplished after every interval.

Results and discussion

The miscut angle α is defined as the angle between the (001) crystal plane and the vicinal surface, which is cut toward the

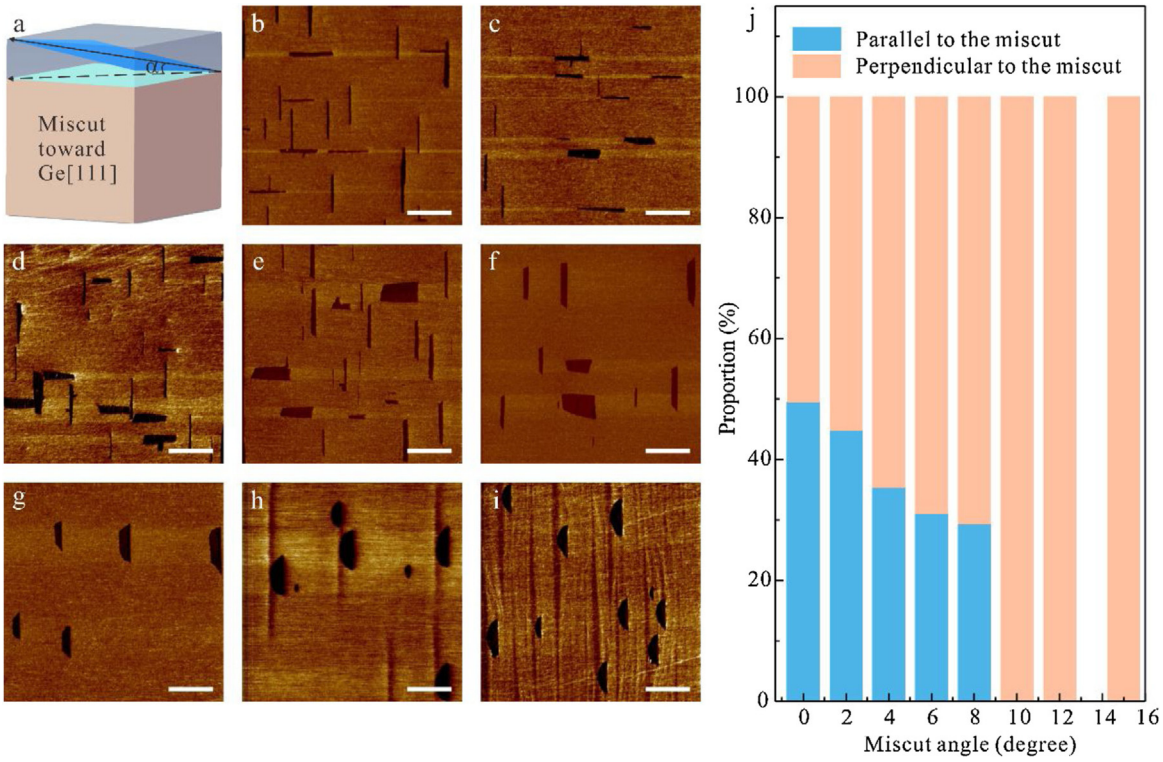

Fig. 1. (a) Schematic diagram of the vicinal Ge(001) surface with a miscut angle of α degree toward Ge[111] direction. Green plane and blue plane represent the (001) crystal plane and vicinal (001) surface, respectively. (b-i) AFM friction images of the graphene islands nucleated on (b) 0°, (c) 2°, (d) 4°, (e) 6°, (f) 8°, (g) 10°, (h) 12°, and (i) 15° miscut Ge(001) surfaces. (j) Population of graphene islands with different orientations versus miscut angle of the vicinal Ge(001) surface. The scale bars in (b-i) are 400 nm.

[111] direction of (001) oriented Ge substrate, as shown in Fig. 1a. Fig. 1b–i presents the AFM friction images of the GNRs grown on the vicinal Ge(001) substrates with miscut angles varying between 0° and 15°. Consistent with the previous reports [26,27,29,30], the GNRs grown on the Ge(001) surface with 0° miscut angle (Fig. 1b) have two dominant orientations, which are parallel or perpendicular to Ge[110] direction (dashed black arrow in Fig. 1a). Both dominant orientations have the equal probability and all GNRs have high aspect ratios and smooth edges. Besides, there is no significant difference in the shape and dimensions of the GNRs grown along the Ge[110] and Ge[$\bar{1}$ 10] directions. However, the growth behavior of GNRs on the vicinal Ge(001) substrate changes gradually as the miscut angle increases. With the increment of miscut angle, nucleation of GNRs along the miscut orientation is suppressed gradually, which finally leads to exclusive population of GNRs perpendicular to the miscut direction (solid black arrow in Fig. 1a). For instance, the percentages of GNRs perpendicular to the miscut orientation on the 2°, 4°, 6°, and 8° miscut Ge(001) surfaces are 55 %, 65 %, 69 %, and 71 %, respectively (Fig. 1j). In particular, when the miscut angle of the vicinal Ge(001) substrate is 10° or above, only graphene islands perpendicular to the miscut direction are formed. As the miscut angle increases from 0° to 15°, the nucleation behavior of GNRs changes from two orthogonal directions to single identical direction. GNRs with two orthogonal directions can further develop and merge into a monolayer polycrystalline graphene wafer consisting of numerous GBs, while well-aligned GNRs are able to evolve into a monolayer single-crystal graphene wafer without GBs [24,25], as compared in Fig. S1.

To understand the influence of the miscut angle on the alignment of GNRs and study the growth mechanism of GNRs on the vicinal Ge(001) surface, density-functional theory (DFT) calculations are performed. For Ge surface cut along (001) crystal plane, each surface Ge atom has two dangling bonds which are able to bind with the dangling bonds of the neighboring Ge atoms and form a Ge-Ge dimer. Here, the direction along the Ge-Ge dimer is defined as a dimer direction, and the perpendicular direction is defined as a dimer row direction. As shown in Fig. 2a, there are four different binding sites for GNRs on the reconstructed vicinal Ge(001) surface based on the binding direction and position. Step-I and Terrace-I represent binding sites along the dimer direction with binding positions at step and terrace, respectively. And, Step-II and Terrace-II are along the dimer row direction with binding sites at step and terrace, respectively. Given that the main edge of GNR on Ge surface is armchair [26], only armchair edged GNRs, rather than zigzag edged GNRs, are considered in our calculations. The formation energy of GNR binding at different sites, E_f(GNR), is defined as follows:

$$E_f(GNR) = E_{Ge\text{-}GNR} - E_{GNR} - E_{Ge} + E_f(AC) \quad (1)$$

where $E_{Ge\text{-}GNR}$ is the energy of the combined system, E_{Ge} is the energy of the Ge substrate, E_{GNR} is the energy of the GNR, and E_f(AC) is the formation energy of the armchair edge in vacuum. DFT calculations show that graphene edges binding at Step-I and Terrace-I possess the formation energies of about 0.1 eV/Å, which is lower than that at Step-II and Terrace-II (Fig. 2b). Therefore, due to the lower formation energy, graphene islands are favorable to bind at the Step-I or Terrace-I sites, rather than Step-II and Terrace-II. The improved stability of graphene islands nucleated at Step-I or Terrace-I sites can be understood by the strong binding between C atoms at the graphene armchair edge and surface Ge atoms, as schematically drawn in Fig. 2c. When the armchair edge of graphene interacts with Ge atoms along the dimer direction, two dangling bonds of the sp^2 hybrid C atom at the graphene edge can be well passivated by both dangling bonds of the surface Ge atoms, leading to a strong GNR-Ge binding configuration formed between the graphene armchair edge and Ge substrate (Step-I or Terrace-I). However, when the armchair edge of graphene interacts with the Ge atoms along the dimer row direction, two dangling bonds of the C atoms at the graphene edge are passivated by only one dan-

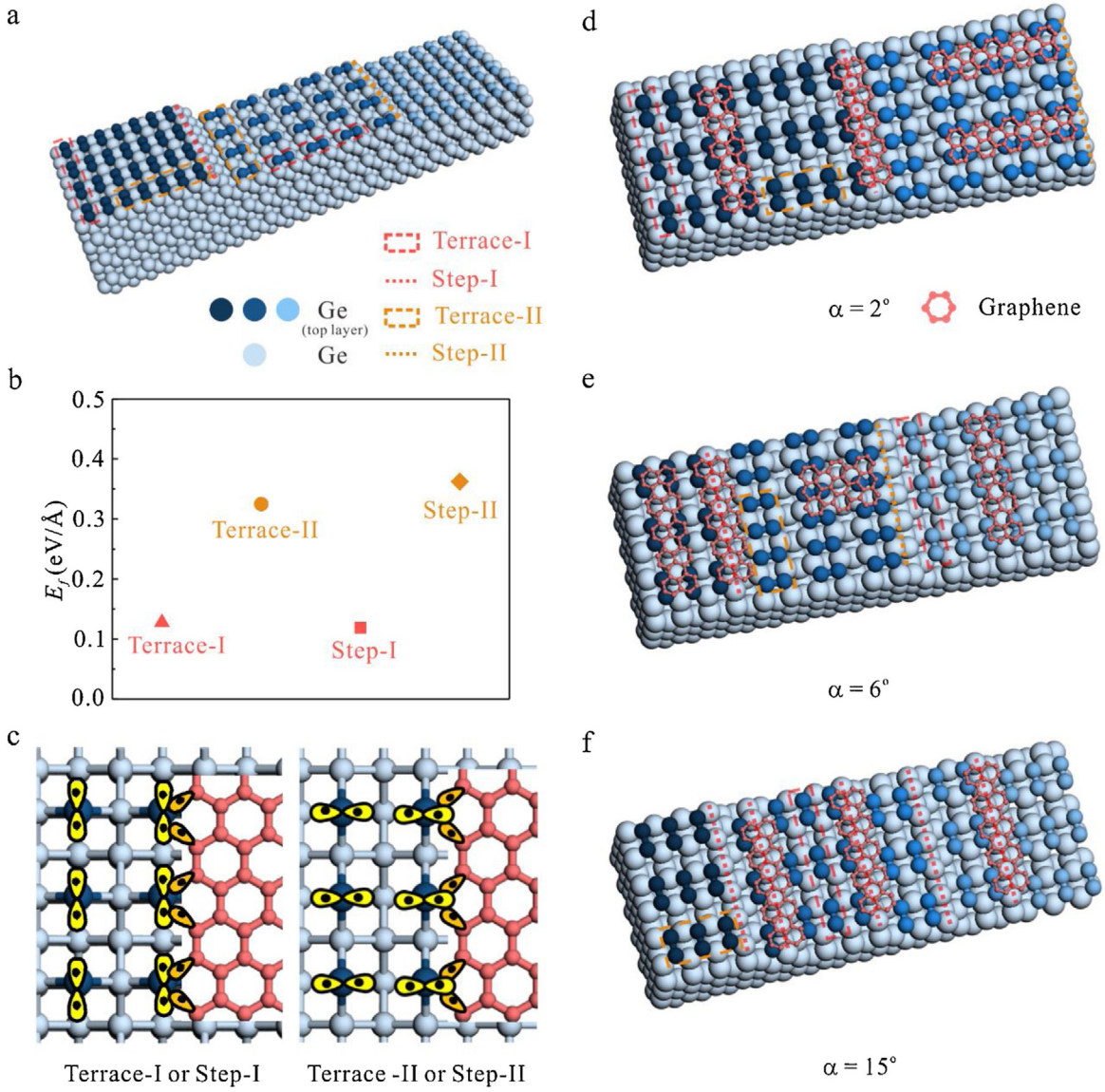

Fig. 2. (a) Schematic atomic structures of the steps and terraces on the vicinal Ge(001) surface. (b) Formation energies of graphene armchair edges binding at the Ge steps and terraces shown in (a). (c) Schematic drawing of the bonds formed between the graphene armchair edge and Ge steps or terraces. Reconstructed surface structures, and growth of GNRs (red atoms) on the vicinal Ge(001) surface with miscut angles of (d) 2°, (e) 6° and (f) 15°, respectively. Different terraces on the vicinal Ge(001) surface are distinguished by different blue atoms.

gling bond of the surface Ge atoms, thus resulting in a weak binding between the graphene armchair edge and Ge substrate (Step-II or Terrace-II). Meanwhile, the preferred nucleations of GNRs at the Terrace-I and Step-I sites with the formation GNR-Ge bonding configurations are also suggested by the calculated phase diagram (Fig. S2). Such an anisotropic surface structure leads to different diffusion behavior of carbon precursor for graphene growth. The diffusion of carbon precursor along the dimer direction is always much faster than that along the dimer row orientation due to the shorter distance between the dangling bonds at the neighboring Ge atoms.

It is well known that the surface structure of the vicinal Ge(001) surface highly depends on the miscut angle, and larger miscut angle usually results in narrower terraces with higher density, which share the same reconstruction orientation of Ge surface atoms (Fig. S3). Fig. 2d–f shows the growth of GNRs on the vicinal Ge(001) surface with miscut angles of 2°, 6°, and 15°, respectively. The vicinal Ge(001) surface with 2° miscut angle is mainly composed of wide terrace structures with alternative reconstruction orientations of Ge surface atoms (Fig. S3a). GNRs grown on this surface have two dominant orientations with similar populations due to the equivalent formation energies of GNRs at Terrace-I/Step-I on the upper terrace and Terrace-I on the lower terrace, and the sufficient carbon precursors diffuse along the dimer direction, as displayed in Fig. 2d. With the increment of miscut angles, the terraces become narrower and more steps appear (Fig. S3b). Due to the reduced width of the terrace, nucleation of GNRs with the orientation parallel to the miscut direction is restricted, because the carbon precursors required for the nucleation is highly reduced due to the limited diffusion space along the miscut orientation (the fast diffusion orientation of carbon precursor). Therefore, the population of GNRs with the orientation parallel to the miscut direction shrinks correspondingly (Fig. 2e). In particular, when the miscut angle is further increased to 15°, the terraces between steps become extremely narrow and the vicinal surface is dominated by dense terraces with the similar Ge reconstruction orientation (Fig. S3c). Therefore, the nucleations of GNRs along the miscut direction are completely suppressed, whereas the formation of GNRs perpendicular to the miscut direc-

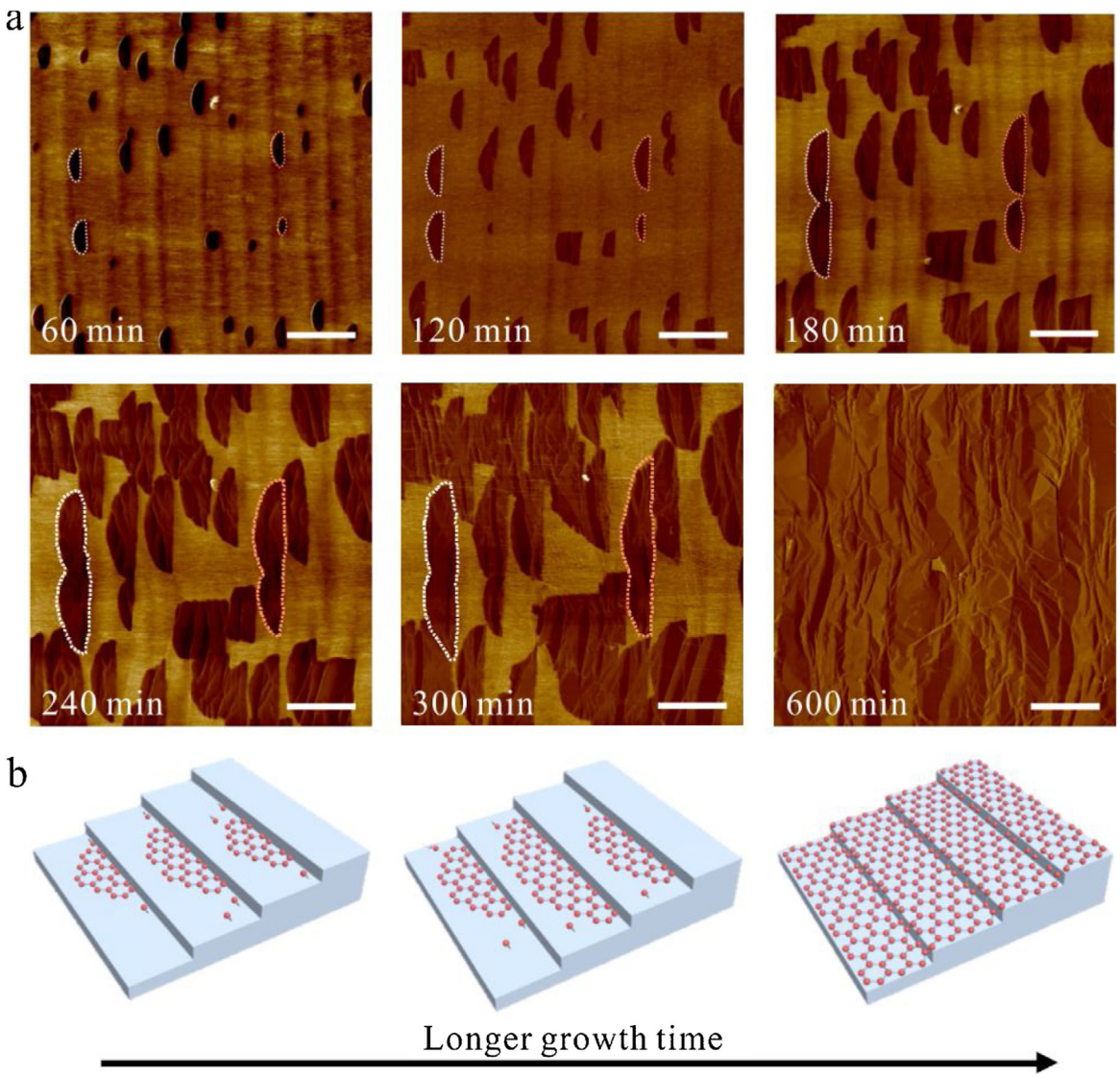

Fig. 3. (a) *Ex situ* AFM observations showing the evolution of graphene islands on the 15° miscut Ge(001) surface after 60 min, 120 min, 180 min, 240 min, 300 min, and 600 min, respectively. (b) Schematic representations illustrating the growth process of single-crystal monolayer graphene film on the 15° miscut Ge(001) surface. The scale bars in (a) are 400 nm.

tion will not be affected, which yields the unidirectional alignment of GNRs grown on the vicinal Ge(001) surface with the 15° miscut angle (Fig. 2f).

To monitor the consecutive growth of graphene and in particular the seamless stitching of the unidirectional graphene islands on the 15° miscut Ge(001) surface, *ex situ* observations are ingeniously designed using the mechanically exfoliated graphene sheets as markers. Using the graphene sheet mounted on the Ge substrate as a position marker (Fig. S4), the sequential AFM tests are able to focus on the identical region adjacent to the marker to monitor the morphology evolution of the graphene islands after multiple growth processes. Fig. 3a displays a sequence of AFM friction images of the graphene islands at different growth stages. For a growth time of 60 min, the graphene islands are observed to nucleate at the atomic steps with the unidirectional orientation. All graphene islands have a semicircular shape and the average aspect ratio is about 2.54. As the growth time extends to 120 min, the sizes of graphene islands further increase, as evident by the expansion of dotted contour lines of graphene islands. The adjacent graphene islands start to coalesce at 180 min and merge at 240 min. As the growth time is extended to 600 min, a continuous graphene film is formed on the 15° miscut Ge(001) surface. Under the proper growth conditions, no additional graphene nucleation is observed and all the initiative graphene islands are maintained with the alignment perpendicular to the miscut direction. The graphene islands with the unidirectional alignment merge seamlessly to form a continuous single-crystal monolayer graphene film without any GBs on the 15° miscut Ge(001) surface, as schematically drawn in Fig. 3b. The observation is different from the graphene film grown directly on the Ge(001) surface without a miscut angle, on which GNRs with two growth orientations lead to the formation of polycrystalline graphene consisting of numerous GBs (Figs. S1 and S5).

HR-TEM and SAED are conducted to confirm the crystalline quality of the CVD grown graphene film on the 15° miscut Ge(001) substrate. Fig. 4a shows the SEM image of the large-area graphene film (>3 mm) transferred to a TEM grid and Fig. 4b shows the atomic-resolution TEM image of the transferred graphene, which clearly reveals the perfect honeycomb lattice of graphene without any defects and vacancies. The band intensity ratio (zone labeled by blue rectangle in Fig. 4d) of ~1:2 suggests the formation of single-layer graphene (Fig. 4c), which is verified by Raman and AFM measurements (Fig. S6). Nine SAED patterns are obtained from nine

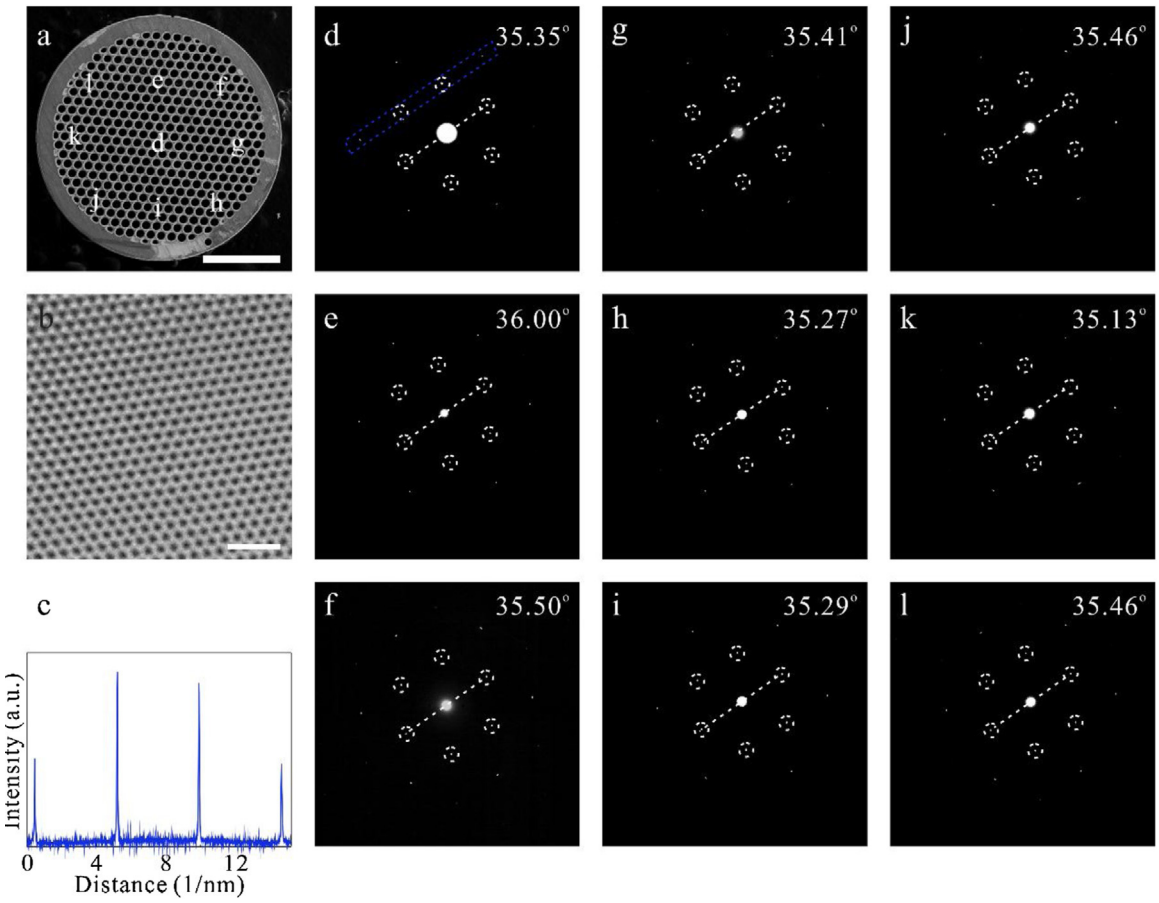

Fig. 4. (a) SEM image of a continuous graphene film transferred onto a TEM grid with the areas marked d-l indicating the regions where multiple SAED patterns are obtained. The scale bar is 1 mm. (b) HR-TEM image of the single-crystal monolayer graphene film showing a defect-free honeycomb lattice (Scale bar =1 nm). (c) Intensity profile of the diffraction spots in the blue rectangle in (d). (d-l) SAED patterns acquired from nine regions indicated in (a).

different regions distributed across the large-area graphene film, as shown in Fig. 4d–l. Each SAED pattern shows a uniform six-fold symmetry with a perfect coincidence (35.5° ± 0.5°), demonstrating the single-crystal nature of the monolayer graphene film.

In addition to the crystalline quality characterization, THz-TDS is performed to determine the carrier mobility across the graphene on the intrinsic 4-inch 15° miscut Ge(001) wafer. THz-TDS is a non-contact and nondestructive approach for rapid determining the carrier mobility of low dimensional materials [37–39], especially applicable to the graphene directly grown on semiconducting substrate [40]. Fig. 5a shows the transmitted THz transient from the graphene/15° miscut Ge(001) as well as a comparison with that from the 15° miscut Ge(001) reference. The THz beam is sensitive to free carriers in the graphene film and the sheet conductance of graphene, $\tilde{\sigma}_s(f)$, can be extracted using the following frequency-dependent transmission function [37]:

$$\sim T_{graphene}(f)=\frac{\sim E_{graphene}(f)}{\sim E_{sub}(f)}=\frac{1+\sim n_{sub}}{1+\sim n_{sub}+Z_0\sim\sigma_s(f)}=\frac{1}{1+\frac{Z_0\sim\sigma_s(f)}{1+\sim n_{sub}}} \quad (2)$$

where $\tilde{E}_{graphene}(f)$ and $\tilde{E}_{sub}(f)$ are the Fast Fourier Transforms (FFT) of the THz waveforms transmitted through the graphene/15° miscut Ge(001) and 15° miscut Ge(001) reference, respectively. The constant $\tilde{n}_{sub}$= 4.1 denotes the THz refractive index of the 15° miscut Ge(001) substrate and $Z_0 = 377\Omega$ is the impedance of free space. To determine the mobility of the graphene film, it is necessary to apply a time domain window to the raw transmitted THz signals to avoid the disturbances of noise (Fig. S7) and use the DC-conductance (σ_{DC}) and carrier scattering rate (τ_{sc}) to fit the Drude model to the real part of the resulting frequency dependent complex conductance of graphene (Fig. 5b). The Drude model is given by

$$\sim\sigma_s(\omega)=\frac{\sigma_{DC}}{1-i\Omega\tau_{sc}} \quad (3)$$

where the angular frequency $\omega = 2\pi f$. The drift mobility (μ_{drift}) of graphene can be calculated by the following relationship [37]:

$$N_s=\frac{\pi\hbar^2}{e^4v_F^2}\left(\frac{\sigma_{DC}}{\tau_{sc}}\right)^2 \quad (4)$$

$$\mu_{drift}=\frac{\sigma_{DC}}{eN_s}=\frac{e^3v_F^2}{\pi\hbar^2}\frac{\tau_{sc}^2}{\sigma_{DC}} \quad (5)$$

where N_s and v_F are the carrier density of graphene and Fermi velocity with a constant value of 10^6 m/s, respectively. By fitting the Drude model to the conductance spectra across the graphene wafer with 1 mm step size, σ_{DC} and μ_{drift} can be mapped, as shown in Figs. S8 and 5 c, respectively. The entire graphene wafer displays a relatively homogenous carrier mobility and over 70 % of the area shows a value larger than 2×10^4 cm^{2}V^{-1}s^{-1}. Fig. 5d shows the histograms of the measured drift mobility that exhibits a Gaussian distribution with an average value of ~4.37×10^4 cm^{2}V^{-1}s^{-1}, which may degrade with the decrease of miscut angle of vicinal Ge(001) substrate (Fig. S9). Considering that THz-TDS is a nondestructive approach for mobility characterization and no transfer process is required, the carrier mobility of the single-crystal graphene grown on 15° miscut Ge(001) substrate is comparable to that of other single-crystal graphene films grown on metal substrates (Table S2).

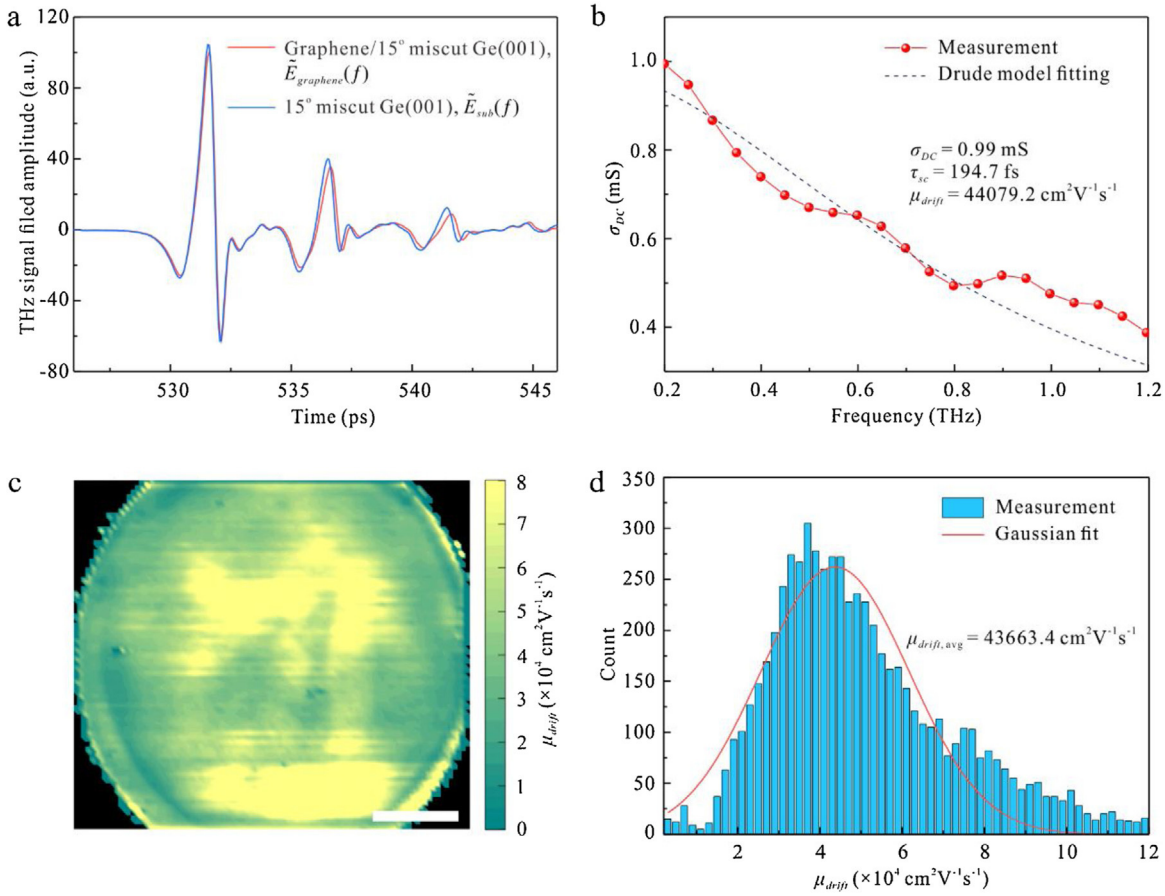

Fig. 5. (a) Waveform of THz transients after transmission through the 15° miscut Ge(001) substrates with and without graphene coverage. (b) DC-conductance spectrum of graphene grown on the 15° miscut Ge(001) surface extracted from (a) with a fitting to Drude model. (c) THz wafer-scale mobility mapping of the graphene film on the 15° miscut Ge(001) wafer (Entire 4-inch graphene wafer raster-mapped with a 1 mm step. The scale bar is 20 mm). (d) Histograms of drift mobility distribution collected from (c).

Conclusions

In conclusion, the alignment of graphene islands closely correlates to the miscut angle of the vicinal Ge(001) substrate, and wafer-scale single-crystal monolayer graphene film can be synthesized by the seamless stitching of aligned graphene islands on the vicinal Ge(001) substrate with the miscut angle of 15°. Theoretical calculations together with *ex situ* AFM observations reveal that the unidirectional alignment of graphene islands on the vicinal Ge(001) surface with large miscut angle is attributed to the suppression of graphene nucleation parallel to the miscut direction, and all aligned graphene islands are perpendicular to the miscut direction. Our study provides a practical approach to manipulate the alignment of graphene islands on vicinal Ge(001) substrate, which is also expected to be applied to other 2D material system including hBN. It may pave the way for commercial production of wafer-scale single-crystal 2D materials and accelerate their application into nanoelectronic devices and circuits in the near future.

Author Contributions

P.L. and W.W. contributed equally to this work. Z.D. and Q.Y. supervised the project. Z.D., M.Z., X.X. and P.L. conceived and designed the experiments. Z.D. and P.L. synthesized the graphene samples and carried out the experimental measurements. Q.Y. and W.W. performed the DFT calculations. Z.D., Q.Y., Y.M., P.L. and P. C. analyzed the data and co-wrote the paper. All the authors discussed the results and commented on the manuscript.

Declaration of Competing Interest

The authors declare no competing financial interest.

Acknowledgements

The authors thank Key Research Project of Frontier Science, Chinese Academy of Sciences (QYZDB-SSW-JSC021), National Science and Technology Major Project (2016ZX02301003), National Natural Science Foundation of China (Grant Nos. 51925208, 61851401, 61774163, 61974157, and 21673075), Science and Technology Commission of Shanghai Municipality (18511110700), Strategic Priority Research Program (B) of the Chinese Academy of Sciences (XDB30030000), Australian Research Council through the Discovery Early Career Research Program (DE170101403), and City University of Hong Kong Strategic Research Grants (SRG) (Grant Nos. 7005105 and 7005264). The computation was performed at the ECNU Multifunctional Platform for Innovation (001) and Shanghai Supercomputer Center.

References

[1] Q. Yu, L.A. Jauregui, W. Wu, R. Colby, J. Tian, Z. Su, H. Cao, Z. Liu, D. Pandey, D. Wei, T.F. Chung, P. Peng, N.P. Guisinger, E.A. Stach, J. Bao, S.-S. Pei, Y.P. Chen, Nat. Mater. 10 (2011) 443–449.

[2] D.L. Duong, G.H. Han, S.M. Lee, F. Gunes, E.S. Kim, S.T. Kim, H. Kim, Q.H. Ta, K.P. So, S.J. Yoon, S.J. Chae, Y.W. Jo, M.H. Park, S.H. Chae, S.C. Lim, J.Y. Choi, Y.H. Lee, Nature 490 (2012) 235–239.

[3] A.W. Tsen, L. Brown, M.P. Levendorf, F. Ghahari, P.Y. Huang, R.W. Havener, C.S. Ruiz-Vargas, D.A. Muller, P. Kim, J. Park, Science 336 (2012) 1143–1146.
[4] R. Ma, Q. Huan, L. Wu, J. Yan, W. Guo, Y.-Y. Zhang, S. Wang, L. Bao, Y. Liu, S. Du, S.T. Pantelides, H.-J. Gao, Nano Lett. 17 (2017) 5291–5296.
[5] K.W. Clark, X.-G. Zhang, I.V. Vlassiouk, G. He, R.M. Feenstra, A.-P. Li, ACS Nano 7 (2013) 7956–7966.
[6] D.V. Tuan, J. Kotakoski, T. Louvet, F. Ortmann, J.C. Meyer, S. Roche, Nano Lett. 13 (2013) 1730–1735.
[7] J. Xu, G. Yuan, Q. Zhu, J. Wang, S. Tang, L. Gao, ACS Nano 12 (2018) 4529–4535.
[8] S. Zhang, L. Gao, A. Song, X. Zheng, Q. Yao, T. Ma, Z. Di, X.-Q. Feng, Q. Li, Nano Lett. 18 (2018) 6030–6036.
[9] J. Li, X.-Y. Wang, X.-R. Liu, Z. Jin, D. Wang, L.-J. Wan, J. Mater. Chem. C 3 (2015) 3530–3535.
[10] X. Xu, Z. Zhang, J. Dong, D. Yi, J. Niu, M. Wu, L. Lin, R. Yin, M. Li, J. Zhou, S. Wang, J. Sun, X. Duan, P. Gao, Y. Jiang, X. Wu, H. Peng, R.S. Ruoff, Z. Liu, D. Yu, E. Wang, F. Ding, K. Liu, Sci. Bull. 62 (2017) 1074–1080.
[11] R. Wu, J. Pan, X. Ou, Q. Zhang, Y. Ding, P. Sheng, Z. Luo, Nanoscale 9 (2017) 9631–9640.
[12] D. Yi, D. Luo, Z.-J. Wang, J. Dong, X. Zhang, M.-G. Willinger, R.S. Ruoff, F. Ding,Phys. Rev. Lett. 120 (2018), 246101.
[13] B. Huet, J.-P. Raskin, Nanoscale 10 (2018) 21898–21909.
[14] X. Xu, Z. Zhang, L. Qiu, J. Zhuang, L. Zhang, H. Wang, C. Liao, H. Song, R. Qiao, P. Gao, Z. Hu, L. Liao, Z. Liao, D. Yu, E. Wang, F. Ding, H. Peng, K. Liu, Nat. Nanotechnol. 11 (2016) 930–935.
[15] C. Liu, X. Xu, L. Qiu, M. Wu, R. Qiao, L. Wang, J. Wang, J. Niu, J. Liang, X. Zhou, Z. Zhang, M. Peng, P. Gao, W. Wang, X. Bai, D. Ma, Y. Jiang, X. Wu, D. Yu, E. Wang, J. Xiong, F. Ding, K. Liu, Nat. Chem. 11 (2019) 730–736.
[16] Y. Cheng, H. Bi, X. Che, W. Zhao, D. Li, F. Huang, J. Mater. Chem. A 7 (2019) 18373–18379.
[17] D. De Fazio, D.G. Purdie, A.K. Ott, P. Braeuninger-Weimer, T. Khodkov, S. Goossens, T. Taniguchi, K. Watanabe, P. Livreri, F.H.L. Koppens, S. Hofmann, I. Goykhman, A.C. Ferrari, A. Lombardo, ACS Nano 13 (2019) 8926–8935.
[18] N. Liu, L. Fu, B. Dai, K. Yan, X. Liu, R. Zhao, Y. Zhang, Z. Liu, Nano Lett. 11 (2011) 297–303.
[19] G. Wang, M. Zhang, S. Liu, X. Xie, G. Ding, Y. Wang, P.K. Chu, H. Gao, W. Ren, Q. Yuan, P. Zhang, X. Wang, Z. Di, Adv. Funct. Mater. 25 (2015) 3666–3675.
[20] M. Huang, M. Biswal, H.J. Park, S. Jin, D. Qu, S. Hong, Z. Zhu, L. Qiu, D. Luo, X. Liu, Z. Yang, Z.L. Liu, Y. Huang, H. Lim, W.J. Yoo, F. Ding, Y. Wang, Z. Lee, R.S. Ruoff, ACS Nano 12 (2018) 6117–6127.
[21] T. Wu, X. Zhang, Q. Yuan, J. Xue, G. Lu, Z. Liu, H. Wang, H. Wang, F. Ding, Q. Yu, X. Xie, M. Jiang, Nat. Mater. 15 (2016) 43–47.
[22] X. Zhang, T. Wu, Q. Jiang, H. Wang, H. Zhu, Z. Chen, R. Jiang, T. Niu, Z. Li, Y. Zhang, Z. Qiu, G. Yu, A. Li, S. Qiao, H. Wang, Q. Yu, X. Xie,Small 15 (2019), 1805395.
[23] G. Wang, M. Zhang, Y. Zhu, G. Ding, D. Jiang, Q. Guo, S. Liu, X. Xie, P.K. Chu, Z. Di, X. Wang, Sci. Rep. 3 (2013) 2465.
[24] J.-H. Lee, E.K. Lee, W.-J. Joo, Y. Jang, B.-S. Kim, J.Y. Lim, S.-H. Choi, S.J. Ahn, J.R. Ahn, M.-H. Park, C.-W. Yang, B.L. Choi, S.-W. Hwang, D. Whang, Science 344 (2014) 286–289.
[25] J. Dai, D. Wang, M. Zhang, T. Niu, A. Li, M. Ye, S. Qiao, G. Ding, X. Xie, Y. Wang, P.K. Chu, Q. Yuan, Z. Di, X. Wang, F. Ding, B.I. Yakobson, Nano Lett. 16 (2016) 3160–3165.
[26] R.M. Jacobberger, B. Kiraly, M. Fortin-Deschenes, P.L. Levesque, K.M. McElhinny, G.J. Brady, R.R. Delgado, S.S. Roy, A. Mannix, M.G. Lagally, P.G. Evans, P. Desjardins, R. Martel, M.C. Hersam, N.P. Guisinger, M.S. Arnold, Nat. Commun. 6 (2015) 8006.
[27] B. Kiraly, A.J. Mannix, R.M. Jacobberger, B.L. Fisher, M.S. Arnold, M.C. Hersam, N.P. Guisinger,Appl. Phys. Lett. 108 (2016), 213101.
[28] A.M. Scaparro, V. Miseikis, C. Coletti, A. Notargiacomo, M. Pea, M. De Seta, L. Di Gaspare, ACS Appl. Mater. Interfaces 8 (2016) 33083–33090.
[29] R.M. Jacobberger, E.A. Murray, M. Fortin-Deschênes, F. Göltl, W.A. Behn, Z.J. Krebs, P.L. Levesque, D.E. Savage, C. Smoot, M.G. Lagally, P. Desjardins, R. Martel, V. Brar, O. Moutanabbir, M. Mavrikakis, M.S. Arnold, Nanoscale 11 (2019) 4864–4875.
[30] P. Li, T. Wang, Y. Yang, Y. Wang, M. Zhang, Z. Xue, Z. Di,Phys. Status Solidi RRL 14 (2019), 1900398.
[31] G. Kresse, J. Furthmüller, Comput. Mater. Sci. 6 (1996) 15–50.
[32] J.P. Perdew, K. Burke, M. Ernzerhof, Phys. Rev. Lett. 77 (1996) 3865–3868.
[33] L. Liu, D.A. Siegel, W. Chen, P. Liu, J. Guo, G. Duscher, C. Zhao, H. Wang, W. Wang, X. Bai, K.F. McCarty, Z. Zhang, G. Gua, PNAS 111 (2014) 16670–16675.
[34] J. Kang, W. Liu, D. Sarkar, D. Jena, K. Banerjee,Phys. Rev. X 4 (2014), 031005.
[35] Y. Gao, S. Kim, S. Zhou, H.-C. Chiu, D. Nélias, C. Berger, W. de Heer, L. Polloni, R. Sordan, A. Bongiorno, E. Riedo, Nat. Mater. 14 (2015) 714–721.
[36] P. Jia, W. Chen, J. Qiao, M. Zhang, X. Zheng, Z. Xue, R. Liang, C. Tian, L. He, Z. Di, X. Wang, Nat. Commun. 10 (2019) 3127.
[37] J.D. Buron, D.M.A. Mackenzie, D.H. Petersen, A. Pesquera, A. Centeno, P. Bøggild, A. Zurutuza, P.U. Jepsen, Opt. Express 23 (2015) 30721–30729.
[38] P.R. Whelan, K. Iwaszczuk, R. Wang, S. Hofmann, P. Bøggild, P.U. Jepsen, Opt. Express 25 (2017) 2725–2732.
[39] R. Dong, P. Han, H. Arora, M. Ballabio, M. Karakus, Z. Zhang, C. Shekhar, P. Adler, P.S. Petkov, A. Erbe, S.C.B. Mannsfeld, C. Felser, T. Heine, M. Bonn, X. Feng, E. Cánovas, Nat. Mater. 17 (2018) 1027–1032.
[40] H. Lin, P. Braeuninger-Weimer, V.S. Kamboj, D.S. Jessop, R. Degl'Innocenti, H.E. Beere, D.A. Ritchie, J.A. Zeitler, S. Hofmann, Sci. Rep. 7 (2017) 10625.

Panlin Li received the B.S. degree from the Department of Material Science and Engineering, Nanchang University, Nanchang, China, in 2015. He is currently a Ph.D. candidate at Shanghai Institute of Microsystem and Information Technology, Chinese Academy of Sciences (CAS), Shanghai, China. His current research interests focus on the synthesis of two-dimensional materials.

Wenya Wei received the B.S. degree from the Department of Physics and Engineering, Zhengzhou University, Zhengzhou, China, in 2015. She is currently a Ph.D. candidate at East China Normal University, Shanghai, China. Her research interests mainly focus on the growth mechanism and electronic properties of two-dimensional materials.

Miao Zhang received the Ph.D. degree from the Shanghai Institute of Microsystem and Information Technology, Chinese Academy of Sciences (CAS), Shanghai, China, in 1998. She is currently a Professor at Shanghai Institute of Microsystem and Information Technology, CAS. Her current research interests include high mobility semiconductors, silicon-on-insulator materials, etc.

Yongfeng Mei received the Ph.D. degree from the City University of Hong Kong, Hong Kong, in 2005. He is currently a Full Professor in Materials Chemistry and Physics at the Department of Materials Science, Fudan University, Shanghai, China. His current research interests include novel inorganic nanomembranes.

Paul K. Chu received the Ph.D. degree in chemistry from Cornell University, Ithaca, NY, USA. He is currently the Chair Professor in Materials Engineering at the Department of Physics and Materials Science, City University of Hong Kong, Hong Kong. His current research interests include plasma surface engineering, materials science, etc.

Xiaoming Xie received the Ph.D. degree from the Shanghai Institute of Microsystem and Information Technology, Chinese Academy of Sciences (CAS), Shanghai, China, in 1990. He is currently a Professor at Shanghai Institute of Microsystem and Information Technology, CAS. His current research interests include novel two-dimensional materials, superconductors, etc.

Qinghong Yuan received the Ph.D. degree from The Chinese University of Hong Kong, Hong Kong, in 2010. In 2012 she joined the Department of Physics at East China Normal University and was promoted to a Full Professor in 2015. She is currently working in the University of Queensland as a DECRA research fellow. Her current research interests focus on theoretical study of the chemical vapor deposition growth of graphene and carbon nanotubes, structure of property investigation of new nanomaterials, surface catalysis, etc.

Zengfeng Di received the Ph.D. degree from the Shanghai Institute of Microsystem and Information Technology, Chinese Academy of Sciences (CAS), Shanghai, China, in 2006. He is currently a Professor at Shanghai Institute of Microsystem and Information Technology, CAS. His current research interests include ion beam technology, silicon-on-insulator materials, low dimensional maaterials, advanced microelectronic devices etc.